Journal of Computational Physics 398 (2019) 108903

Contents lists available at ScienceDirect

Journal of Computational Physics

www.elsevier.com/locate/jcp

A coupled immersed interface and grid based particle method for three-dimensional electrohydrodynamic simulations

Shih-Hsuan Hsu [a], Wei-Fan Hu [b,*], Ming-Chih Lai [a]

[a] Department of Applied Mathematics, National Chiao Tung University, 1001, Ta Hsueh Road, Hsinchu 300, Taiwan
[b] Department of Applied Mathematics, National Chung Hsing University, 145, Xingda Road, Taichung 402, Taiwan

ARTICLE INFO

Article history:
Received 19 February 2019
Received in revised form 5 August 2019
Accepted 17 August 2019
Available online 22 August 2019

Keywords:
Elliptic interface problem
Immersed interface method
Grid based particle method
Electrohydrodynamics
Electrorotation
Chaotic tumbling motion

ABSTRACT

In the present work, we propose a coupled immersed interface and grid based particle method to solve two-phase electrohydrodynamic problems in three dimensions. The problem considers a leaky dielectric (weakly conducting) droplet immersed in another leaky dielectric fluid under electric field where the non-homogeneous droplet surface charge effect is taken into account. Due to the mismatch of electrical properties between two fluids, the electric potential satisfying Laplace equation with jump conditions across the droplet surface is coupled with the conservation equation for the surface charge density. Consequently, we first develop a three-dimensional augmented immersed interface method (IIM) which incorporates some known jump conditions naturally along the normal direction and check the desired accuracy. Here, the grid based particle method (GBPM) is used to track the interface by the projection of the neighboring Eulerian grid points so no requirement for stitching of parameterizations nor body fitted moving meshes. Within the leaky dielectric framework, the electric stress can be treated as an interfacial force so that both the surface tension and electric force can be formulated in a unified continuum force in the Navier-Stokes equations. A series of numerical tests have been carefully conducted to illustrate the accuracy and applicability of the present method to simulate droplet electrohydrodynamics. In particular, we investigate the droplet equilibrium dynamics under weak and strong electric fields in detail. It is interesting to find out a chaotic tumbling motion with irregular rotating modes which we believe that is the first numerical verification to the recent experiments.

1. Introduction

The study of hydrodynamics driven by an electric field (ElectroHydroDynamics, EHD) has received much attention due to its wide industrial applications such as micro-fluidic systems [20], inkjet printing [2], electrospraying [3], just to name a few. In particular, a leaky dielectric (weakly conducting) droplet suspended in another leaky dielectric fluid under electric field has been extensively studied from different perspectives. In the pioneering work of G.I. Taylor [26], he concluded that the equilibrium drop shape can be determined by the balance between the viscous stress and electric stress (which is created due to the mismatch of electric properties between two fluids) along the droplet surface. As the flow is initiated by the externally applied electric field, the hydrodynamics of the system is affected by the interplay between the hydrodynamic

* Corresponding author.
E-mail addresses: narisawa.am02g@g2.nctu.edu.tw (S.-H. Hsu), wfhu@nchu.edu.tw (W.-F. Hu), mclai@math.nctu.edu.tw (M.-C. Lai).

https://doi.org/10.1016/j.jcp.2019.108903
0021-9991/

stress, capillary traction due to surface tension, and the normal electric stress. The droplet can be deformed into either a prolate or an oblate equilibrium shape with circulatory flows inside the droplet at moderate electric intensity, and the flow patterns mainly depend on the electrical conductivity and permittivity of the fluid system. Taylor's theory was able to predict both oblate and prolate shapes and showed a good agreement with experiments in weak electric field. A comprehensive review of further theoretical developments based on small-deformation from a spherical drop can be found in [1,21].

However, in the original Taylor's work, the transient effect of surface charge convection was neglected leading to some inconsistent results compared to the experimental findings [9,23,24]. It was found that when the charge relaxation timescale for the suspending fluid is shorter than the one of the droplet so the surface charge will accumulate on both sides of the droplet surface and the arrangement of surface charge distribution contributes to an oriented electric dipole moment opposite to the electric field. In such circumstance, for sufficiently strong electric field, any small perturbation on the surface charge will break the equilibrium predicted by Taylor's model, leading to a favorable consequential rotational flow (electrorotation) in order to flip the orientation of the induced dipole along the electric field direction. This stable electrorotational motion was also found for an insulated rigid sphere suspending in a weakly conducting fluid (Quincke rotation) [18]. By taking the charge convection into account, Ha and Yang [9] experimentally showed that the threshold electric field strength is dependent on the drop size as well as the viscosity ratio. He et al. [8] also developed a small deformation theory which interprets the experimentally observed non-axisymmetric droplet in a uniform DC electric field. Lanauze et al. [14] implemented a boundary element method in axisymmetric coordinates, and their simulations showed that there is a discrepancy between the results obtained with and without charge convection. In [4], Das and Saintillan derived a second-order accurate small-deformation theory to predict the axisymmetric drop deformation, and they further implemented a three-dimensional boundary integral method mimicking the droplet electrorotation [5]. It is worthy to mention that, by applying a stronger electric field beyond the threshold for electrorotation, Salipante and Vlahovska [24] observed that the droplet can even experience a chaotic rotating motion. To the best of our knowledge, this chaotic phenomenon has not yet been found in any other numerical literature but will be firstly investigated and verified in present numerical simulations.

In this paper, we develop a coupled immersed interface and grid based particle method to simulate the dynamics of a leaky dielectric droplet with presence of electric field in another leaky dielectric fluid in three dimensions. Unlike our previous 2D [6] and axisymmetric work [17], the non-homogeneous droplet surface charge effect is taken into account so the electric potential satisfying Laplace equation with jump conditions across the droplet surface is coupled with the conservation equation of the surface charge density. We exploit the immersed interface method to solve the potential problem since the electric potential and its derivatives can be discontinuous across the droplet surface owing to the different electric properties. To discretize the Laplace equation for the electric potential, a simple finite difference method is used so that fast direct solver can be applied straightforwardly. We take advantage of using the grid based particle method (GBPM) [11] to represent the interface (droplet surface). In the framework of GBPM, the interface is tracked via finding the closest points (on the interface) of the Eulerian gird points in a small neighborhood of the surface. In this manner, all geometrical quantities (such as the mean curvature and the distance between the grid point to the interface) can be computed accurately by a local coordinates construction. Moreover, the correction terms used in immersed interface discretization for electric potential requiring the surface derivatives at the closest points can also be done easily in the GBPM setting. As in our previous 2D work for droplet and vesicle electrohydrodynamics [6,7], the electric effect is cast as an interfacial electric force (the jump of Maxwell stress tensor across the interface) so that the surface tension and electric force can be unified as a continuum force in the full Navier-Stokes equations.

The paper is organized as follows. The mathematical model for the droplet electrohydrodynamics within the leaky dielectric framework with surface charge convection is presented in Section 2. An efficient 3D immersed interface method for solving the electric potential equation with jump conditions is introduced and the code verification is performed in Section 3. The full numerical algorithm coupling IIM and GBPM for solving the droplet electrohydrodynamics is outlined in Section 4. A series of numerical simulations to investigate the droplet equilibrium shapes in weak and strong electric fields is given in Section 5. Some concluding remarks and future work are given in Section 6.

2. Mathematical model for droplet electrohydrodynamics

2.1. Setup of the problem

Consider a leaky dielectric droplet immersed in another leaky dielectric fluid under an external electric field $\mathbf{E}_\infty = (0, 0, E_\infty)$. Initially, the droplet is in equilibrium shape as a sphere with minimal surface tension energy. Denoting the droplet surface by Σ which separates the fluid domain inside (Ω^-) and outside (Ω^+) of the droplet so that the entire physical domain is $\Omega = \Omega^- \cup \Omega^+$. The fluid electric properties such as conductivity and permittivity are defined by σ and ε, respectively. We denote μ^-, σ^- and ε^- as the fluid viscosity, conductivity and permittivity of the droplet, and μ^+, σ^+ and ε^+ of the suspending fluid. The ratios of these three quantities are given by $\mu_r = \mu^-/\mu^+$, $\sigma_r = \sigma^-/\sigma^+$, and $\varepsilon_r = \varepsilon^-/\varepsilon^+$. One can see the problem setup as in Fig. 1.

The interface (droplet surface) representation is modeled by the GBPM [11] in which an evolving surface is tracked by the combination of Eulerian and Lagrangian approaches. Precisely, the moving interface is represented by a set of meshless particles (or Lagrangian markers) which are the *closest points* obtained by finding the orthogonal projections from the Eulerian grids in a small neighborhood of the surface (see Fig. 2 for 2D illustration). For a point $\mathbf{x} \in \Omega$, we use the notation

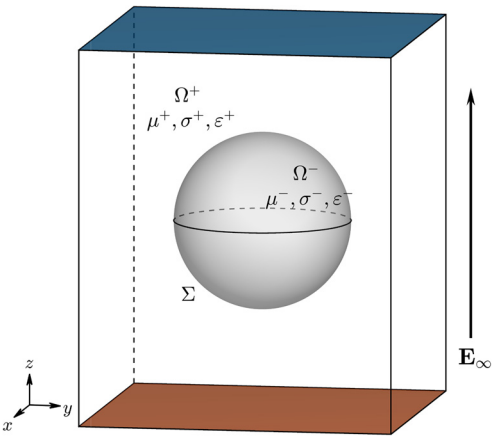

Fig. 1. A leaky dielectric drop suspended in another leaky dielectric fluid under DC electric field. μ^-, σ^-, ε^- correspond to the viscosity, electric conductivity, electric permittivity of the droplet, and μ^+, σ^+, ε^+ of the suspending fluid.

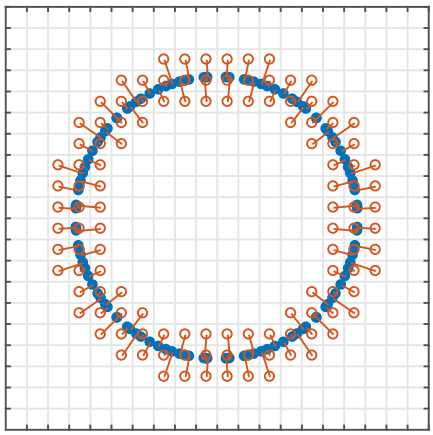

Fig. 2. The interface representation based on GBPM. In this case the interface is a circle while the red points denote the Eulerian grid points and the blue markers are the closest points (Lagrangian markers) corresponding to those Eulerian grid points. (For interpretation of the colors in the figure(s), the reader is referred to the web version of this article.)

$\mathbf{x}^{cp}$ as its closest point on the surface Σ; all interfacial variables will be defined at the set formed by the closest points. Of course, one shall resample those closest points when the interface is moving, see the details in [11]. Using such an underlying Eulerian grid reference can avoid the re-meshing process for the usual Lagrangian-based tracking method [22,28] and is capable of dealing with topological change of interfaces [11]. In addition, we take advantage of GBPM which naturally incorporates those closest points originating from Eulerian grids so that the computations of geometrical quantities and surface derivatives needed in present immersed interface method can be performed easily. This point will become clear in our later discussion.

2.2. Governing equations

As the flow is initiated by the applied electric field, the droplet electrohydrodynamics is determined by the interaction between the hydrodynamics, surface tension, and electric stresses defined on the droplet surface Σ. For simplicity, we assume that the drop is neutrally buoyant (the density ρ interior and exterior to the droplet surface are identical) in the fluid domain Ω and the gravitational force is neglected. As aforementioned, the droplet surface Σ is represented by the unstructured Lagrangian markers denoted by $\mathbf{X}(=\mathbf{x}^{cp})$. The two-fluid system is governed by the three-dimensional dimensionless incompressible Navier-Stokes equations with the applied electric field $\mathbf{E}_\infty$ as

$$\frac{\partial \mathbf{u}}{\partial t} + (\mathbf{u}\cdot\nabla)\mathbf{u} = -\nabla p + \frac{1}{Re}\nabla\cdot(2\mu D) + \mathbf{f} \quad \text{in } \Omega, \tag{1}$$

$$\nabla\cdot\mathbf{u} = 0 \quad \text{in } \Omega, \tag{2}$$

$$\frac{\partial \mathbf{X}}{\partial t} = \mathbf{u}(\mathbf{X}, t) \quad \text{on } \Sigma, \tag{3}$$

where $\mathbf{u}$ is the fluid velocity, p is the pressure, $D = \frac{1}{2}(\nabla\mathbf{u} + \nabla\mathbf{u}^T)$ is the deformation tensor. Eq. (3) simply states that the Lagrangian markers on the droplet surface move along with the local no-slip fluid velocity $\mathbf{u}(\mathbf{X}, t) = \mathbf{U}$. Here, the Reynolds number is defined by $Re = \frac{\rho a^2}{\mu^+ T_{MW}}$ in which a and $T_{MW} = \frac{\varepsilon^- + 2\varepsilon^+}{\sigma^- + 2\sigma^+}$ stand for the initial droplet radius and Maxwell-Wagner polarization time, respectively. The viscosity $\mu(\mathbf{x}) = \mu_r$ and $\mu(\mathbf{x}) = 1$ correspond to its values inside and outside of the droplet surface Σ. The external forcing term consisting of the forces due to the surface tension and electric stress is given by

$$\mathbf{f}(\mathbf{x}, t) = \left(\frac{1}{Re\,Ca}\mathbf{F}_\gamma + \frac{1}{Re\,Ma}\mathbf{F}_E\right)\delta(d(\mathbf{x}, t)), \tag{4}$$

where δ stands for the Dirac delta function and d is the signed distance function measuring from $\mathbf{x}$ to its closest point $\mathbf{x}^{cp}$ on the surface. Notice that in the present model, this singular force is treated in a sense of continuum surface force in the entire physical domain Ω thus $\mathbf{f}(\mathbf{x})$ is simply evaluated by $\mathbf{f}(\mathbf{x}^{cp})$. The dimensionless capillary number is given by $Ca = \frac{\mu^+ a}{\gamma T_{MW}}$ with the surface tension γ and the Mason number $Ma = \frac{\mu^+}{\varepsilon^+ T_{MW} E_\infty^2}$. The above non-dimensionalization can be found in [5].

The surface tension force in Eq. (4) reads

$$\mathbf{F}_\gamma = -2H\mathbf{n}, \tag{5}$$

where H is the mean curvature and $\mathbf{n}$ is the unit outward normal vector on Σ. The electric stress in a dielectric medium under an electric field is given by the Maxwell stress tensor which takes the form [15]

$$\mathbf{M}_E = \varepsilon\left(\mathbf{E}\otimes\mathbf{E} - \frac{1}{2}(\mathbf{E}\cdot\mathbf{E})I\right). \tag{6}$$

Since the permittivity ε and electric field $\mathbf{E}$ are discontinuous across the droplet surface, as in our previous work for the two-dimensional droplet and vesicle electrohydrodynamics [6,7], the electric effect can be regarded as an interfacial force arising from the normal jump of the Maxwell tensor. That is,

$$\mathbf{F}_E = [\![\mathbf{M}_E\cdot\mathbf{n}]\!] = (\mathbf{M}_E^+ - \mathbf{M}_E^-)\cdot\mathbf{n}, \tag{7}$$

where the bracket $[\![\cdot]\!]$ stands for the jump of the quantity approaching from the Ω^+ side to the Ω^- side. In the following subsection, we will address how to find the electric field $\mathbf{E}$ in the domain Ω.

2.3. Leaky dielectric model with surface charge convection

Since both fluids occupying interior and exterior domain of the droplet are weakly conducting dielectric mediums, we adopt the leaky dielectric model proposed by G.I. Taylor [15]. That is, we assume the charge relaxation time is much shorter compared to the characteristic fluid relaxation time. Consequently, the electric field is quasistatic and irrotational ($\nabla\times\mathbf{E} = \mathbf{0}$), and can be expressed in terms of $\mathbf{E} = -\nabla\phi$, in which ϕ is the electric potential satisfying the Laplace equation

$$\Delta\phi = 0 \quad \text{in } \Omega\backslash\Sigma. \tag{8}$$

The above Laplace equation is accompanied with the vanished jump condition due to continuity of the electric potential across the interface

$$[\![\phi]\!] = 0 \quad \text{on } \Sigma. \tag{9}$$

Unlike the previous work for 2D [6] and axisymmetric [17] droplet case in which the normal component of ohmic current $\mathbf{J} = \sigma\mathbf{E}$ is assumed to be continuous across the interface (i.e. $[\![\sigma\nabla\phi\cdot\mathbf{n}]\!] = [\![\sigma\phi_n]\!] = 0$, ϕ_n is the shorthand notation for $\nabla\phi\cdot\mathbf{n}$ throughout), here we take the imbalanced ohmic current due to the surface charge convection into account. Thus, the conservation of surface charge density can be written as

$$\frac{DQ_s}{Dt} + (\nabla_s\cdot\mathbf{U})Q_s = \frac{1}{Re_E}[\![\sigma\phi_n]\!] \quad \text{on } \Sigma, \tag{10}$$

where the surface charge density is defined as $Q_s = -[\![\varepsilon\phi_n]\!]$ and $Re_E = \frac{\varepsilon^+}{\sigma^+ T_{MW}}$ is the electric Reynolds number. The material derivative is defined by $\frac{D}{Dt} = \frac{\partial}{\partial t} + \mathbf{u}\cdot\nabla$ and $\nabla_s\cdot$ is the surface divergence operator. While the simplified Taylor's model (by assuming $[\![\sigma\phi_n]\!] = 0$) only leads to a toroidal flow inside of the droplet thus attaining axisymmetric equilibrium shapes, recent experimental results [23,24] have revealed that the spontaneous rotational flow with non-axisymmetric shape can be found for the droplet under stronger electric field in which the surface charge convection plays a significant role. This is exactly what we pursue in this paper and is the major difference between the present work and our previous 2D and axisymmetric results in [6,17]. The remaining issue is how to solve the elliptic interface problem in Eq. (8) subject to the jump conditions in Eqs. (9)-(10).

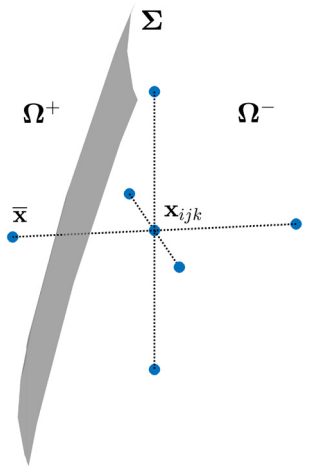

Fig. 3. The seven-point Laplacian at the irregular point $\mathbf{x}_{ijk}$.

3. A 3D immersed interface method for solving elliptic interface problem

The immersed interface method is known to be a sharp interface method being capable of capturing the solution discontinuity across interfaces, see the book [13] for more details and its wide applications. In this section, we aim to develop a numerical method based on IIM framework to solve the potential satisfying the Poisson equation with general inhomogeneous jump conditions as

$$\Delta\phi = f \quad \text{in } \Omega, \quad [\![\phi]\!] = g, \quad [\![\varepsilon\phi_n]\!] = w \quad \text{on } \Sigma. \tag{11}$$

Notice that, here we assume both the jump discontinuities are given on Σ (rather than coupled with the time-evolutional equation as in Eq. (10) where $[\![\varepsilon\phi_n]\!]$ is not known a priori). The present 3D immersed interface method for solving Eq. (11) is extended mainly from the one developed in [29,6] for two dimensions. Despite with a similar spirit to our 2D counterpart, the fully 3D numerical scheme bears more complicated implementation details such as finding the projection of grid points on the surface and evaluating the Laplace-Beltrami operator on the surface as we can see later.

To proceed, let us first layout a uniform Cartesian grid in the computational domain Ω^h with the mesh width $h = \Delta x = \Delta y = \Delta z$ for simplicity. The grid point $\mathbf{x}_{ijk}$ is located at the cell center where the discrete solution $\phi_{ijk} = \phi(\mathbf{x}_{ijk})$ is defined. The embedding interface (or surface) Σ cuts through some grid cells so the potential solution is not smooth across the interface. We categorize the grid point as either a regular or irregular point. For a regular point, it means that the standard seven-point Laplacian discretization (denoted by Δ^h) in Eq. (11) does not cut through the interface so the second-order local truncation error is achieved. On the other hand, at an irregular point, the seven-point Laplacian cuts through the interface so the used grid points involve both inside and outside of the interface (see Fig. 3, for instance). Since the solution and its derivatives have jump discontinuities across the interface, a correction for the Laplacian discretization is needed at the irregular point to maintain the desired accuracy. As a result, the discretization for the Poisson equation in Eq. (11) at a grid point $\mathbf{x}_{ijk}$ can be generally written in the form of

$$\Delta^h\phi_{ijk} + \frac{C_{ijk}}{h^2} = f_{ijk} \quad \text{in } \Omega^h, \tag{12}$$

where the term C_{ijk} is the correction and is nonzero only at irregular points.

Next, let us describe what the correction term should be at this particular irregular point as depicted in Fig. 3. When we apply the seven-point Laplacian to $\mathbf{x}_{ijk}$, only the grid point $\bar{\mathbf{x}}$ belongs to the different side of the interface so the correction of discretization arises only from the point $\bar{\mathbf{x}}$. (More points in different side are similarly treated in a point-by-point manner.) By applying Taylor's expansion at the closest point $\bar{\mathbf{x}}^{cp}$ (the projection point of $\bar{\mathbf{x}}$ on the interface) along the normal direction, one can easily derive the correction term as

$$C_{ijk} = [\![\phi]\!] + d[\![\phi_n]\!] + \frac{d^2}{2}\left([\![f]\!] - 2H[\![\phi_n]\!] - \Delta_s[\![\phi]\!]\right)\Big|_{\bar{\mathbf{x}}^{cp}}, \tag{13}$$

where $d = d(\bar{\mathbf{x}})$, and H is the mean curvature of the interface. Notice that, the closest point $\bar{\mathbf{x}}^{cp}$ and the mean curvature at $\bar{\mathbf{x}}^{cp}$ can be evaluated easily using the present GBPM to represent the interface. (This is one of the reason why we choose GBPM to represent the interface in this paper.) It can be seen that the seven-point Laplacian discretization in Eq. (12) with the correction term in Eq. (13) gives second-order accuracy at regular points whereas only first-order accuracy at irregular

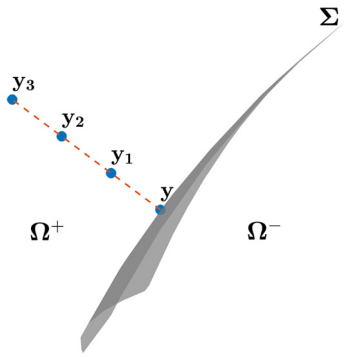

Fig. 4. The normal derivative of $\phi_n^+(\mathbf{y})$ is computed by one-sided extrapolation using the values of $\phi(\mathbf{y}_1), \phi(\mathbf{y}_2)$ and $\phi(\mathbf{y}_3)$.

ones. Notice that the correction involves the computation of the surface Laplacian (or Laplace-Beltrami) operator $\Delta_s[\![\phi]\!]$ at closest points, this step can be conveniently done via a normal extension to the jump $[\![\phi]\!]$ with second-order accuracy, see the closest point method in [19] for detailed implementations.

Since all the terms on the righthand side of Eq. (13) are basically available except the normal derivative jump $[\![\phi_n]\!]$ at the closest point $\overline{\mathbf{x}}^{cp}$, it is quite natural to relate the given jump condition $[\![\varepsilon\phi_n]\!]$ with $[\![\phi_n]\!]$ using either one of the formulas as in [12]

$$\phi_n^+ + \frac{\varepsilon^-}{[\![\varepsilon]\!]}[\![\phi_n]\!] = \frac{[\![\varepsilon\phi_n]\!]}{[\![\varepsilon]\!]} \quad \text{if } \varepsilon_r(=\varepsilon^-/\varepsilon^+) > 1, \quad \text{or} \quad \phi_n^- + \frac{\varepsilon^+}{[\![\varepsilon]\!]}[\![\phi_n]\!] = \frac{[\![\varepsilon\phi_n]\!]}{[\![\varepsilon]\!]} \quad \text{if } \varepsilon_r < 1. \tag{14}$$

Here ϕ_n^+ and ϕ_n^- are both normal derivatives at the closest point $\overline{\mathbf{x}}^{cp} = \mathbf{y}$ approaching from the outside and inside of the interface, respectively. For succinctness, we will just describe how to approximate the outer normal derivative ϕ_n^+ in the following since the similar approximation can be applied to ϕ_n^- too. Here, we use the one-sided extrapolation formula in [29] to approximate the outer normal derivative as

$$\phi_n^+(\mathbf{y}) = \frac{-5\phi(\mathbf{y}_1) + 8\phi(\mathbf{y}_2) - 3\phi(\mathbf{y}_3)}{2h}, \tag{15}$$

where $\mathbf{y}_\ell = \mathbf{y} + \ell h\mathbf{n}(\mathbf{y})$ for $\ell = 1, 2, 3$ and $\mathbf{n}(\mathbf{y})$ is the outward normal vector at $\mathbf{y}$, see the illustration in Fig. 4. One can carefully check that the above extrapolation for the derivative gives a local truncation error of magnitude $O(h^2)$. However, the values of $\phi(\mathbf{y}_\ell)$ obviously do not coincide with grid values ϕ_{ijk}, hence a local second-degree Lagrange interpolation must be adopted to find $\phi(\mathbf{y}_\ell)$ using the grid values ϕ_{ijk} nearby $\mathbf{y}_\ell$. (Notice that, the error induced by the interpolation is $O(h^3)$ leading to a consistent truncation error $O(h^2)$ in Eq. (15)). It might be possible that the Lagrange interpolation at $\mathbf{y}_\ell$ adopts the grid point values lying on different side of the interface, especially when the closest point $\mathbf{y}$ locates at a high curvature region. For instance, the grid points used to interpolate $\phi(\mathbf{y}_1)$ fall into both sides of the interface. Then we have to choose the grid points that are slightly away from $\mathbf{y}_1$ but fall into the same side of the interface so that the Lagrange polynomial of degree two can be constructed. In practice, one can just use the same grid points to interpolate $\phi(\mathbf{y}_1)$ and $\phi(\mathbf{y}_2)$ to simplify the interpolating process since $\mathbf{y}_2$ appears to be further away from the interface than the interpolating point $\mathbf{y}_1$.

3.1. Implementation details

Let us denote Φ and Ψ by the solution vectors formed from ϕ_{ijk} and $[\![\phi_n]\!]_{\overline{\mathbf{x}}^{cp}}$, respectively. The discrete equation (12) with the correction term (13) results in a matrix equation as

$$A\Phi + C\Psi = F, \tag{16}$$

where A is the matrix version of seven-point Laplacian, and C is the formal matrix operator involving the correction term described previously. The righthand side vector F simply results from f_{ijk}, the boundary conditions for ϕ, and those given correction terms related to $[\![\phi]\!]$ and $[\![f]\!]$ at closest points. At closest points, the discretization for Eq. (14) is represented by

$$B^{\pm}\Phi + \frac{\varepsilon^{\mp}}{[\![\varepsilon]\!]}\Psi = W, \tag{17}$$

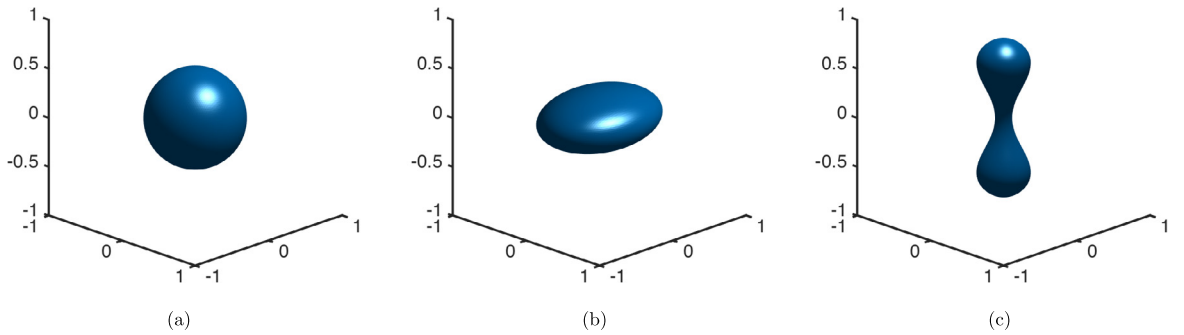

Fig. 5. Three chosen surfaces: (a) A sphere. (b) An ellipsoid. (c) A peanut-like surface.

where B^+ and B^- denote the formal matrices arising from the one-sided normal derivative approximation (introduced in previous subsection) along the outward and inward directions, respectively. Combining Eq. (16) and (17), the resultant linear system becomes

$$\begin{bmatrix} A & C \\ B^{\pm} & \frac{\varepsilon^{\mp}}{[\![\varepsilon]\!]} I \end{bmatrix} \begin{bmatrix} \Phi \\ \Psi \end{bmatrix} = \begin{bmatrix} F \\ W \end{bmatrix}. \tag{18}$$

In practice, we do not form the matrices A, $B^{\pm}$ and C explicitly as we can see from the following iterative procedure of our linear system solver. The above linear system is solved by Schur complement technique (after some careful matrix calculations) via the following three steps:

Step 1. Apply one fast Poisson solver to obtain the intermediate solution Φ^* in

$$A\Phi^* = F.$$

Step 2. Apply GMRES iterative method to solve Ψ in

$$\left(B^{\pm}A^{-1}C - \frac{\varepsilon^{\mp}}{[\![\varepsilon]\!]} I\right)\Psi = B^{\pm}\Phi^* - W.$$

Here, we set the stopping criteria for GMRES iteration as $h^2/100$ to ensure the second-order accuracy can be achieved.

Step 3. Apply one fast Poisson solver to obtain Φ in

$$A\Phi = F - C\Psi.$$

The overall computational cost for Steps 1-3 in our present scheme can be evaluated in terms of the number of fast Poisson solver being applied.

3.2. Numerical accuracy and efficiency study

We demonstrate the numerical accuracy and efficiency of the developed 3D immersed interface method by solving Eq. (11) with the following analytical solution in $\Omega = [-1, 1]^3$

$$\phi_e(x, y, z) = \begin{cases} \exp(x + y + z) & \text{if } \mathbf{x} \in \Omega^-, \\ \sin(x)\sin(y)\sin(z) & \text{if } \mathbf{x} \in \Omega^+. \end{cases}$$

Here, we choose three different shapes of interface Σ to separate Ω^- and Ω^+ as depicted in Fig. 5 and listed below:

1. A spherical surface centered at the origin with radius 0.5.
2. An ellipsoidal surface centered at origin with semi-principal axes of length 0.7, 0.5 and 0.3.
3. A peanut-like surface parameterized as [32]

$$\left\{ \left(2r(\beta)\cos\theta, 2r(\beta)\sin\theta, \frac{4}{5}\sin\beta\right) \middle| \theta \in [0, 2\pi], \beta \in [-\frac{\pi}{2}, \frac{\pi}{2}] \right\}$$

where $r(\beta) = \left(0.0414 + 0.4006\sin^2\beta - 0.2246\sin^4\beta\right)\cos\beta$.

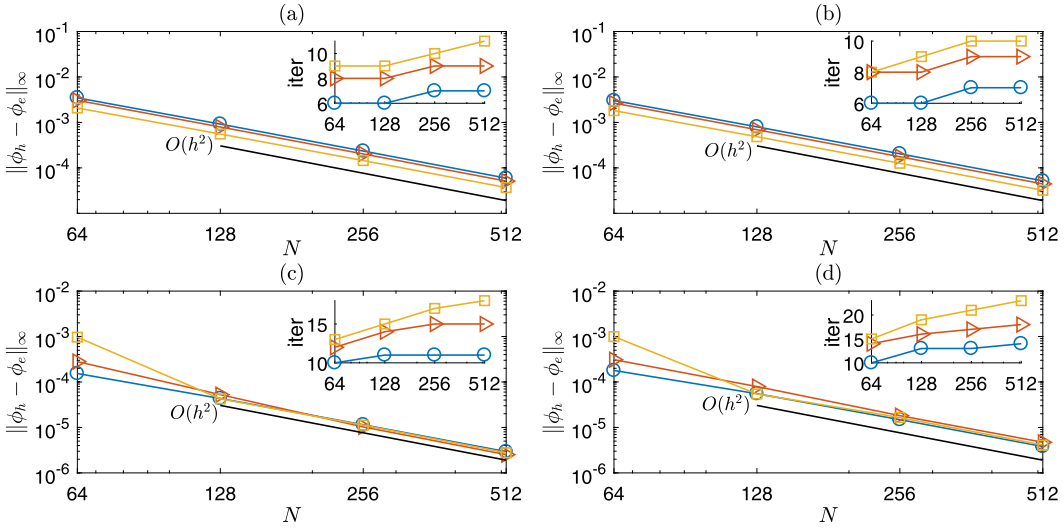

Fig. 6. The mesh refinement results with different surfaces: sphere ('○'), ellipsoid ('▷'), peanut-like surface ('□'). The inset of each figure shows the iteration number of GMRES with different N. (a) $\varepsilon_r = 10^{-2}$. (b) $\varepsilon_r = 10^{-1}$. (c) $\varepsilon_r = 10$. (d) $\varepsilon_r = 10^2$.

Once the analytic solution ϕ_e, the interface Σ, and the piecewise constant coefficients ε are given, one can easily compute the corresponding righthand side function f and the jump conditions g and w from Eq. (11) that are needed in our test inputs.

The computational domain is set by $\Omega^h = [-1, 1]^3$ and N denotes the grid size thus the mesh width is $h = 2/N$ in x-, y-, and z-directions. The Dirichlet boundary condition is imposed on the boundary $\partial\Omega$ just for convenience. Other boundary conditions such as Neumann condition used in later applications can be implemented without any difficulty. Let ϕ_h and ϕ_e be the numerical and analytical solution, respectively. The mesh refinement results are shown in Fig. 6 with different coefficient ratios $\varepsilon_r = \varepsilon^-/\varepsilon^+ = 10^{-2}, 10^{-1}, 10$ and 10^2. The errors for the case of a sphere, an ellipsoid, and a peanut-like surface are denoted by the circle ('○'), triangle ('▷') and square ('□') markers, respectively. The black solid line in the figure stands for the rate with second-order convergence. As one can see, the maximum norm error $\|\phi_h - \phi_e\|_\infty$ converges with second-order accuracy as increasing the grid size for all cases. Different chosen surfaces only produce a small deviation of the errors showing the applicability of the proposed method. The number of GMRES iteration versus grid size for all cases are depicted in the inset of each sub-figure. One can immediately see that the iteration number becomes steady or slightly increasing when the grid size doubles indicating the efficiency of the present method. Notice that, the criterion of choosing the relating formula based on the coefficient ε_r (either greater or smaller than one) in Eq. (14) is critical. If we violate the criterion and choose the formula otherwise, then the GMRES iteration number will be linearly increased as the grid size doubles. We have run all the tests in Fig. 6 again by reversing the choice (for instance, use $\phi_n^+ + \frac{\varepsilon^-}{[\![\sigma]\!]}[\![\phi_n]\!] = \frac{[\![\varepsilon\phi_n]\!]}{[\![\varepsilon]\!]}$ if $\varepsilon_r < 1$). Although the second-order convergence can still be achieved, the number of GMRES iteration increases significantly (compared to the results in Fig. 6), especially when ε_r is larger or smaller. The detailed numerical comparisons are omitted here.

4. Numerical algorithm for solving droplet electrohydrodynamics

In this section, we introduce the entire numerical algorithm for solving the electrohydrodynamic system of Eqs. (1)-(10). The computational domain is set as a cuboid $\Omega = [a_1, a_2] \times [b_1, b_2] \times [c_1, c_2]$. Within this domain, a uniform lattice grid with mesh width h is employed. The velocity components u, v and w are defined at usual staggered grid as

$$(x_{i-1/2}, y_j, z_k) = (a_1 + (i-1)h, b_1 + (j-1/2)h, c_1 + (k-1/2)h),$$
$$(x_i, y_{j-1/2}, z_k) = (a_1 + (i-1/2)h, b_1 + (j-1)h, c_1 + (k-1/2)h),$$
$$(x_i, y_j, z_{k-1/2}) = (a_1 + (i-1/2)h, b_1 + (j-1/2)h, c_1 + (k-1)h),$$

while the pressure p and electric potential ϕ are defined at the cell center labeled as

$$(x_i, y_j, z_k) = (a_1 + (i-1/2)h, b_1 + (j-1/2)h, c_1 + (k-1/2)h).$$

Notice that, the Cartesian grid points used by GBPM to represent the surface are all chosen at cell center points $\mathbf{x}_{ijk} = (x_i, y_j, z_k)$; all interfacial variables will be defined at the resulting closest points generated by $\mathbf{x}_{ijk}$ within a narrow band

nearby the surface. The signed distance function, normal vector, and mean curvature of the surface can be easily obtained by GBPM.

Let Δt be the time step size, and n be the time step index. At the beginning of each time step $t_n = n\Delta t$, the fluid velocity $\mathbf{u}^n$, the interface position $\mathbf{X}^n$, the surface charge density $Q_s^n (= Q_s(\mathbf{X}^n, n\Delta t))$, and all geometrical quantities on the droplet interface Σ^n are computed and given. The advance for one time step can be summarized as follows.

1. Solve the electric potential ϕ^n with the given jump conditions $[\![\phi]\!] = 0$ and $[\![\varepsilon\phi_n]\!] = -Q_s^n$ by the proposed immersed interface method in Section 3.
2. Compute the electric field $\mathbf{E}^n = -\nabla^h\phi^n$ at all closest points and then use them to compute $\mathbf{M}_E^+$ and $\mathbf{M}_E^-$ to obtain the electric force $\mathbf{F}_E^n$. Notice that we apply the standard central difference to compute $\nabla^h\phi^n$ using the computed solutions of two adjacent grid points, which requires a correction at irregular points. This step can be done straightforwardly since the jump $[\![\phi_n]\!]^n$ is also solved in Step 1. After obtaining $\nabla^h\phi^n$ at all grid points, we interpolate these values at the closest points on Σ^n.
3. Compute the surface tension force $\mathbf{F}_\gamma^n$ and electric force $\mathbf{F}_E^n$. Recall that, both singular forces are defined in continuum sense along normal direction so that the total force is computed by
$$\mathbf{f}^n(\mathbf{x}_{ijk}) = \left(\frac{1}{Re\,Ca}\mathbf{F}_\gamma^n + \frac{1}{Re\,Ma}\mathbf{F}_E^n\right)\delta_h(d(\mathbf{x}_{ijk}, t_n)),$$
where the smooth version of delta function δ_h is chosen as in [31]. Since the force $\mathbf{f}^n$ is defined at the cell center $\mathbf{x}_{ijk}$, we need to further interpolate the value at the corresponding velocity grid point used in the following Navier-Stokes solver.
4. Solve the Navier-Stokes equations by the first-order accurate projection method [30] as follows:
$$\frac{\mathbf{u}^* - \mathbf{u}^n}{\Delta t} + (\mathbf{u}^n\cdot\nabla^h)\mathbf{u}^n = -\nabla^h p^n + \frac{1}{Re}\left(\mu^*\Delta^h\mathbf{u}^* - \mu^*\Delta^h\mathbf{u}^n + \nabla^h\cdot(2\mu D)^n\right) + \mathbf{f}^n,$$
$$\Delta^h p^* = \frac{1}{\Delta t}\nabla^h\cdot\mathbf{u}^*, \quad \left.\frac{\partial p^*}{\partial n}\right|_{\partial\Omega} = 0,$$
$$\mathbf{u}^{n+1} = \mathbf{u}^* - \Delta t\nabla^h p^*, \quad \nabla^h p^{n+1} = \nabla^h p^n + \nabla^h p^* - \frac{\mu^*\Delta t}{Re}\Delta^h(\nabla^h p^*),$$
where $\mu^* = \max(1, \mu_r)$. One can immediately see that the above discretization involves solving constant coefficient elliptic equations for the intermediate velocity $\mathbf{u}^*$ and the pressure increment p^* which can be done efficiently by using FFT or fast direct solvers. The viscosity function $\mu(\mathbf{x})$ can be calculated through the harmonic averaging [27] as
$$\frac{1}{\mu(\mathbf{x})} = \frac{H_h(d(\mathbf{x}))}{1} + \frac{1 - H_h(d(\mathbf{x}))}{\mu_r}, \quad H_h(x) = \begin{cases} 0 & \text{if } x < -2h, \\ \frac{1}{2} + \frac{x}{4h} + \frac{1}{2\pi}\sin\left(\frac{\pi x}{2h}\right) & \text{if } -2h \le x \le 2h, \\ 1 & \text{if } x > 2h. \end{cases}$$
Here H_h is the discrete Heaviside function.
5. Interpolate the new velocity $\mathbf{u}^{n+1}$ at the Lagrangian markers $\mathbf{X}^n$ to obtain $\mathbf{U}^{n+1}$. Eq. (10) is solved by an operator splitting technique; that is, we first find the intermediate surface charge Q_s^* by
$$\frac{Q_s^* - Q_s^n}{\Delta t} + (\nabla_s^h\cdot\mathbf{U}^{n+1})Q_s^* = \frac{1}{Re_E}[\![\sigma\phi_n]\!]^n,$$
and then transport Q_s^* along $\mathbf{U}^{n+1}$ ($DQ/Dt = 0$) as we shall see in next step. Notice that Q_s^* is defined at $\mathbf{X}^n$. The computation of the term $\nabla_s^h\cdot\mathbf{U}^{n+1}$ can be simply done by the closest point method, see [19] for detail.
6. Advance the Lagrangian markers to the new interface position $\mathbf{X}^{n+1}$ and then resample the closest points (see the detail in [11]). Next, update the surface charge by assigning Q_s^* to $Q_s^{n+1}(\mathbf{X}^{n+1})$ at the new interface position.

5. Numerical results

In this section, a series of numerical simulations are performed for the droplet EHD system. We adopt the experimental setup of characteristic physical quantities as in [8,23]. In each simulation, unless otherwise stated, we use the electric permittivity $\varepsilon^+ = 4.6927\times10^{-11}$ F/m and $\varepsilon^- = 2.6563\times10^{-11}$ F/m; the electric conductivity $\sigma^+ = 4.5\times10^{-11}$ S/m and $\sigma^- = 1.23\times10^{-12}$ S/m; the fluid viscosity $\mu^+ = 0.69$ Pa s and $\mu^- = 9.74$ Pa s; the density $\rho = 971$ kg/m^3; the surface tension $\gamma = 4.5\times10^{-3}$ N/m. The electric field intensity E_∞ is taken in the range from 8.0339×10^4 to 8.0339×10^5 V/m. Referring to the above physical parameters, we obtain the dimensionless numbers $\mu_r = 14.1$, $\sigma_r = 0.0273$, $\varepsilon_r = 0.566$, $Re_E = 0.79$, $Ma = 0.01725 \sim 1.725$.

It is worthy to mention that, under the present setup $(\sigma_r, \varepsilon_r) = (0.0273, 0.566)$ with moderate Ma numbers, the droplet attains an equilibrium oblate shape while the induced circulatory flow inside the first quadrant of the x-z plane is clockwise (from the pole to the equator) similar to Taylor's asymptotic result. However, the recent experimental findings [23,24]

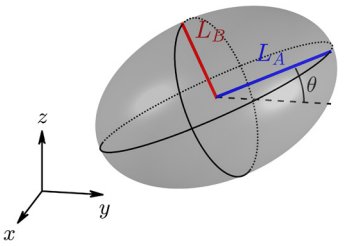

Fig. 7. The droplet deforms into an ellipsoid-like surface due to the external electric field. The length of major and minor axis are given by L_A and L_B respectively. Here θ represents the inclination angle of the droplet.

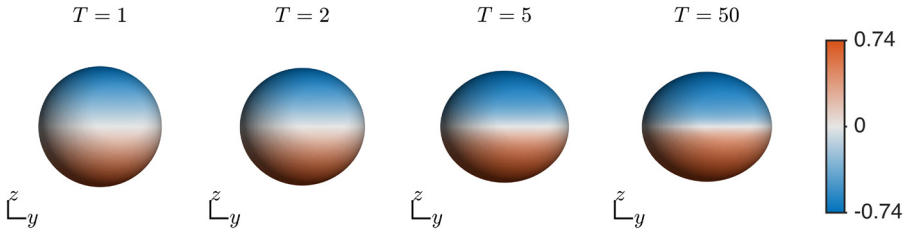

Fig. 8. Time evolutional profiles for the droplet deformation and surface charge density distribution (denoted by color codes) at $\chi = 0.8$. Equilibrium oblate shape is obtained at $T \sim 50$.

showed that a spontaneous electrorotation can take place if the intensity of the external electric field is sufficiently large. This symmetry breaking is due to the charge relaxation time $T_C = \varepsilon/\sigma$ for the bulk fluid is shorter than the one in droplet ($T_C^+ < T_C^-$, which is equivalent to the condition $\sigma_r < \varepsilon_r$). Consequently, the induced electric dipole moment is in opposite direction to the electric field leading to an unfavorable surface charge distribution. Hence, the droplet begins to rotate in order to flip the orientation of the induced dipole along the electric field direction. The similar instability was experimentally found by Quincke [18] for a rigid spherical particle suspended in a weakly conducting fluid. The critical electric field intensity for Quincke rotation was derived in [10,16] as

$$E_Q = \sqrt{\frac{2\sigma^+\mu^+(\sigma_r+2)^2}{3\varepsilon^+\varepsilon^-(1-\sigma_r/\varepsilon_r)}}.$$

The critical value for E_Q in the present case is 2.67×10^5 V/m. We further define the dimensionless electric field intensity $\chi = E_\infty/E_Q$ describing the ratio between the applied and critical electric field for Quincke rotation.

Throughout this paper, all numerical simulations are performed in the dimensionless manner. So initially, we put a unit spherical drop in a quiescent flow with the computational domain $\Omega^h = [-4, 4]^3$. (Note that, the dimensionless length is scaled by the realistic droplet radius a in the paper.) The no-slip boundary condition for the velocity ($\mathbf{u}|_{\partial\Omega} = \mathbf{0}$) is imposed on each wall; the boundary condition for the electric potential is subjected to $\phi = -z$ (Dirichlet) on $z = \pm 4$ so the applied electric field is pointing upward along the z direction. The zero Neumann condition is imposed on $x = y = \pm 4$. We set the grid size $N = 128$ (thus $h = 8/N$) and the time step $\Delta t = h/4$ unless otherwise stated. Each simulation is terminated when the EHD system attains an equilibrium. It is worth mentioning that the domain confinement might affect the equilibrium shape of droplet behavior [25]. In order to properly compare our present simulations with the theoretical and experimental findings in the literature, the present system is set to be a weak confinement with confinement ratio 0.25 (defined by $2a/L$ with channel height L). In the following, we will investigate the effect of applied electric field and viscosity ratio on droplet electrodeformation by the numerical algorithm presented in previous section.

5.1. Effect of electric field intensity

We begin by investigating the effect of electric field intensity with $\chi = 0.8$ and 1.2. In this case, the initial radius of the droplet is set by $a = 1.25$ mm (corresponding to $Re = 1.666 \times 10^{-3}$ and $Ca = 1.452 \times 10^{-1}$). The deformation factor of the droplet is measured by

$$D_f = \frac{L_A - L_B}{L_A + L_B},$$

where L_A and L_B denote the length of the major and minor axis for the droplet correspondingly (see Fig. 7). By setting $\chi = 0.8$, as seen in Fig. 8, the droplet is elongated due to the electric force and reaches a stable equilibrium of oblate shape at $T \sim 50$. The cross-sectional view of the stream line and flow quiver on y-z plane are further depicted in Fig. 9. The circulatory flow pattern is formed inside of the droplet and flows from the pole to the equator of the droplet. This

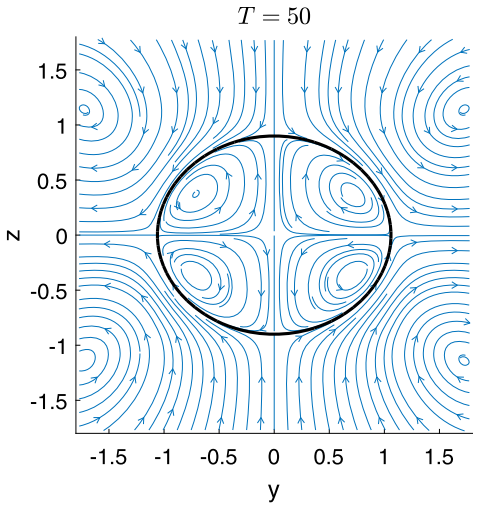

Fig. 9. The cross-sectional view of the flow pattern on the y-z plane at $T = 50$ with $\chi = 0.8$.

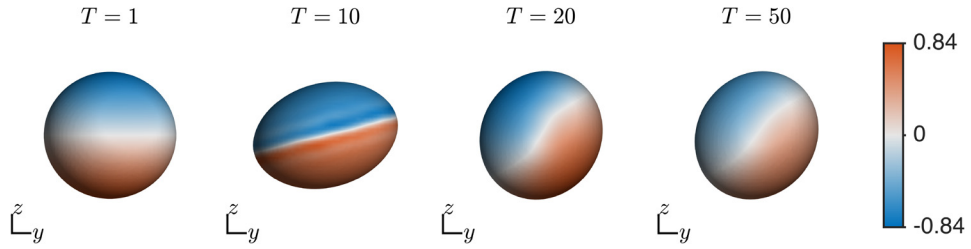

Fig. 10. Time evolutional profiles for the droplet deformation and surface charge density distribution (denoted by color codes) at $\chi = 1.2$. The droplet undergoes a rotational flow and adopts an oblique ellipsoid-like shape as its equilibrium at $T \sim 50$.

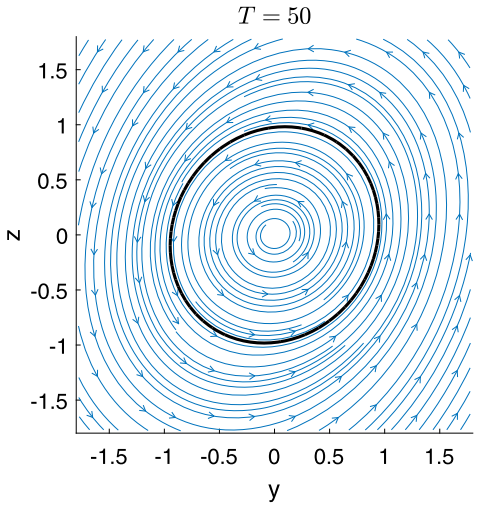

Fig. 11. The cross-sectional view of the flow pattern on the y-z plane at $T = 50$ with $\chi = 1.2$.

flow behavior is predicted by Taylor's leaky dielectric theory. Upon increasing larger $\chi = 1.2$, a bifurcation takes place in which the strong electric field leads to a symmetry breaking of the EHD system. In this scenario, the electric dipole moment is aligned inversely with the electric field, resulting in a spontaneous electrorotation as equilibrium and the droplet is oblique with the tilted angle θ measured by the droplet major axis and the y-axis (see Fig. 7). The time-evolutional electrodeformation of the droplet and distribution of surface charge density are shown in Fig. 10. One can clearly see the stationary rotational flow pattern inside the droplet in Fig. 11.

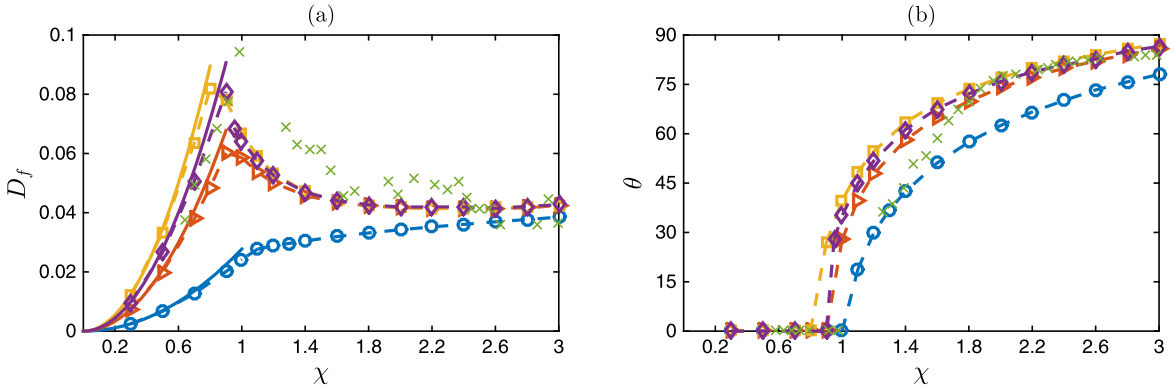

Fig. 12. $a = 0.25$ mm ('○'); $a = 0.75$ mm ('▷'); $a = 1$ mm (◇); $a = 1.25$ mm ('□'); the experiment results [8] with $a = 1$ mm ('×'). (a) The deformation factor D_f versus χ. Solid lines denote the results obtained from Taylor's theory [1]. (b) The tilt angle θ of the droplet versus χ.

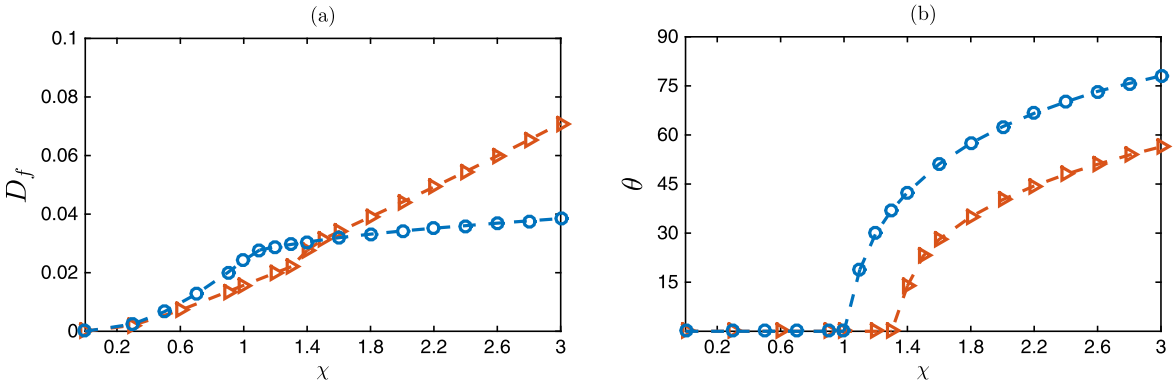

Fig. 13. (a) The deformation factor D_f versus χ. (b) The tilt angle θ of the droplet versus χ. $\mu_r = 14.1$ ('○'); $\mu_r = 1.41$ ('▷').

Moreover, we run a series of numerical simulations with different droplet radius $a = 0.25, 0.75, 1, 1.25$ mm to find the deformation factor and tilt angle as function of χ. From Fig. 12(b), the critical electric intensity χ_c for $a = 0.25$ mm almost coincides with the critical value ($\chi_c \sim 1$) for Quincke rotation. One can further see that as the droplet radius a increases, the critical value χ_c for electrorotation decreases accordingly. This tendency is completely consistent with the experimental results in [9]. More specifically, we plot the deformations obtained by the small deformation theory in [1] with the solid lines in Fig. 12(a). It shows that our numerical solutions agree with the theoretical predictions very well in Taylor's regime when χ is smaller than one, whereas the droplets continue to deform monotonically due to the straining flow when χ exceeds the critical values. Physically speaking, increasing the strength of the electric field χ enhances the electric torque, thus the tilt angle is increased. This can be found for the all cases in Fig. 12(b).

For comparison, we extract the experimental data obtained from the reference [8] for the case of $a = 1$ mm. One can see from Fig. 12(a) that the deformation factor obtained from the numerical result matches well with the one obtained from the experimental data when the dimensionless electric intensity χ is smaller than one. However, some deviation appears when χ is greater than one and the deviation gets smaller when χ becomes larger. In Fig. 12(b), the numerical and experimental results about the tilt angle θ versus the electric intensity χ show a similar tendency as in Fig. 12(a), but both results have a better agreement when χ is large.

5.2. Effect of the viscosity contrast

Now we study the effect of viscosity contrast by repeating the numerical simulations in previous subsection with different viscosity ratios $\mu_r = 14.1$ and 1.41 (for the case $\mu_r = 1.41$ we take $\Delta t = h/8$ to maintain the numerical stability). We set the initial droplet radius $a = 0.25$ mm. The deformation and tilt angle with different electric field intensity χ are shown in Fig. 13 where the circles ('○') give the result obtained by $\mu_r = 14.1$ and triangles ('▷') for $\mu_r = 1.41$. In Fig. 13(b), one can immediately see that the critical threshold χ_c to reach electrorotation for the less viscous droplet ($\mu_r = 1.41$) is larger than the critical one for the more viscous droplet $\mu_r = 14.1$. The droplet is elongated beyond the threshold while the smaller $\mu_r = 1.41$ gives a profound deformation compared to the larger $\mu_r = 14.1$ as shown in Fig. 13(a). Again the droplet tilt angle at equilibrium is monotonically increasing with χ for both μ_r. The tendency of the curve $\theta(\chi)$ in Fig. 13(b) agrees qualitatively with the experimental results in [23].

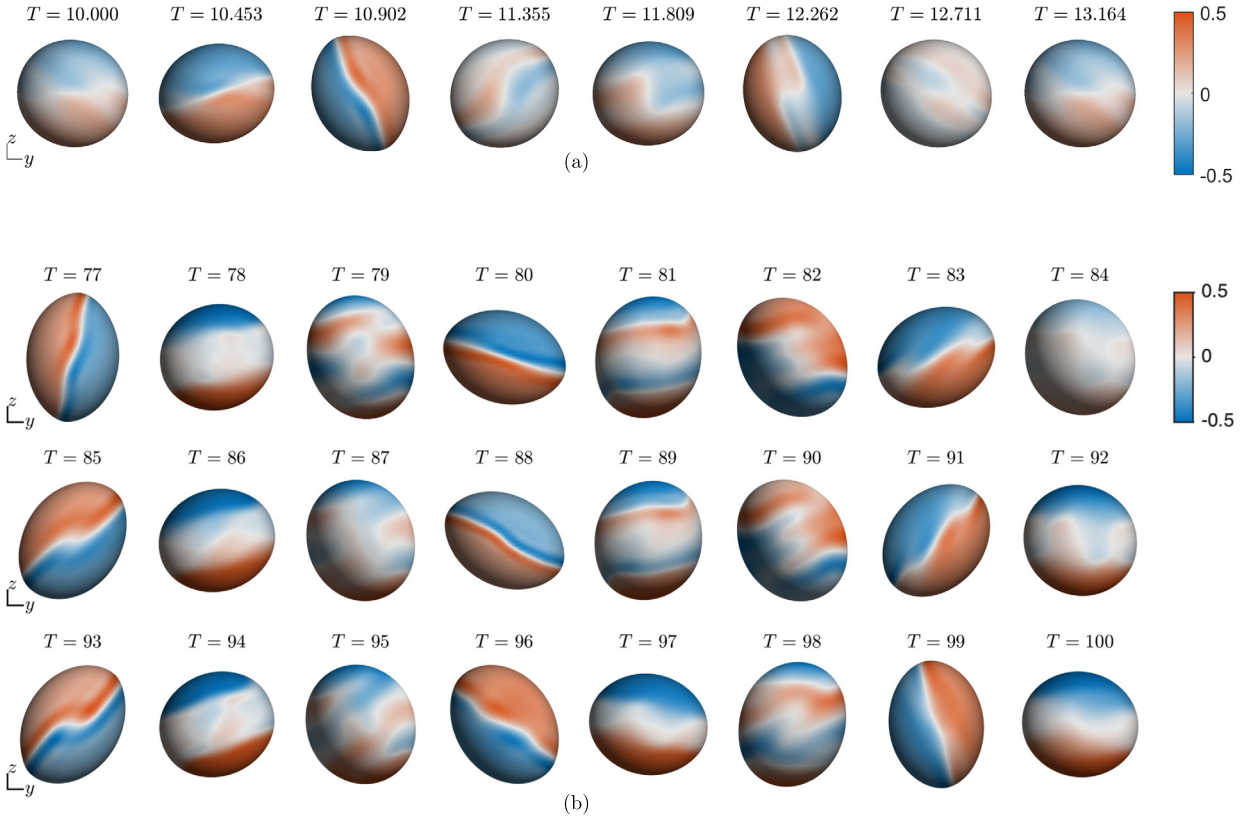

Fig. 14. Transient behavior of the droplet under strong electric field $\chi = 5$; the color coding shows the surface charge density. (a) $\mu_r = 50$: the transient droplet motion is shown in a single period. (b) $\mu_r = 14.1$: the chaotic tumbling motion is found.

5.3. Chaotic electrodynamics under strong electric field

In this subsection, we further increase the electric field to see how the droplet behaves. We enhance the electric field strength to $\chi = 5$ and again set the initial droplet radius $a = 0.25$ mm. To maintain the numerical stability due to the strong electric field, we set the time step $\Delta t = h/16$. We investigate the effect of varying viscosity contrast by setting $\mu_r = 50$ and $\mu_r = 14.1$. Fig. 14 shows the snapshots of the surface charge distribution and electrodeformation of the droplet at different times. It is interesting to see that, at high viscosity ratio $\mu_r = 50$, the droplet undergoes a periodic shape changing and tumbling motion (the period is approximately 3.164). Whereas for the low viscosity case $\mu_r = 14.1$, the shape of droplet varies with time and no certain pattern of droplet motion behavior can be recognized; the ellipsoidal droplet tumbles while irregularly reverses its direction of rotation.

To investigate more carefully, for the both cases, we plot the phase diagram for the deformation and tilt angle $(D_f(t), \theta(t))$ in polar coordinates for $10 \le t \le 100$ (the r-axis denotes the magnitude of $D_f(t)$ and the θ-axis represents the tilt angle $\theta(t)$). As seen in Fig. 15, the phase portrait of the periodic motion for the case of $\mu_r = 50$ converges to a limit cycle. While in the case of viscosity ratio $\mu_r = 14.1$, the trajectory of the orbit passes through the $r - \theta$ space and is quite dense in the map. This kind of characteristic chart indicates that the present EHD system can be chaotic under a strong electric field (if the droplet undergoes a stable electrorotation, there will be a single point in the map). As known, chaotic phenomena for fluid motions are common only when the Reynolds number is large. However, in our current droplet under electric field setting, the fluid electrohydrodynamic system in Stokes regime can undergo chaotic behavior too. To the best of our knowledge, this is the first numerical result showing this kind of chaotic behavior for the droplet rotation under strong electric field which is also observed in experiments [24].

6. Conclusions

In this paper, we have combined the immersed interface method (IIM) and grid based particle method (GBPM) to simulate droplet electrohydrodynamics in three-dimensional Navier-Stokes leaky dielectric fluids. The electric potential is solved numerically by an augmented IIM which incorporates the jump conditions naturally along the normal direction so that the involving correction terms in the IIM can be easily computed thanks to the GBPM representation. The electric effect is treated as an interfacial force with a normal jump due to the Maxwell stress on the surface. Hence, the droplet elec-

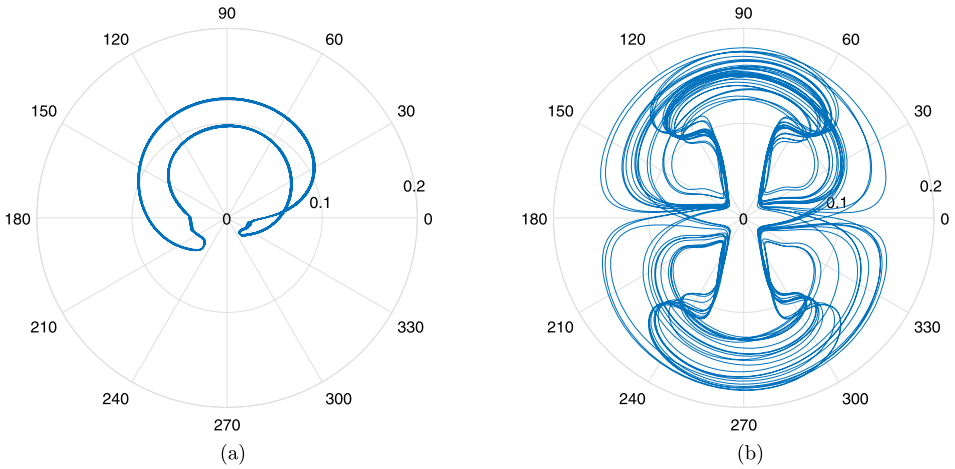

Fig. 15. Phase diagram for $(D_f(t), \theta(t))$ for $10 \le t \le 100$ in polar coordinates at $\chi = 5$. (a) $\mu_r = 50$. (b) $\mu_r = 14.1$.

trohydrodynamics can be cast by the Navier-Stokes equations with external forcing term written in a continuum sense. To carefully verify our numerical algorithms, we first check the accuracy of the present immersed interface method for solving the electric potential. We further investigate how the electric field and viscosity contrast affect the droplet dynamics in equilibrium. By imposing the droplet to a strong electric field, we find that the droplet undergoes a chaotic tumbling motion with oscillatory deformations. In the future, we shall give a systematic study on the route to chaos for this EHD system and explore the multiple droplets interaction by our proposed method.

Declaration of competing interest

The authors declare that they have no known competing financial interests or personal relationships that could have appeared to influence the work reported in this paper.

Acknowledgements

W.-F. Hu acknowledges support by Ministry of Science and Technology, Taiwan under research grant MOST-107-2115-M-005-004-MY2. M.-C. Lai acknowledges support from MOST-107-2115-M-009-016-MY3 and National Center for Theoretical Sciences.

References

[1] O.O. Ajayi, A note on Taylor electrohydrodynamic theory, Proc. R. Soc. Lond. Ser. A 364 (1978) 499.
[2] O.A. Basran, H. Gao, P.P. Bhat, Nonstandard inkjets, Annu. Rev. Fluid Mech. 45 (2013) 85–113.
[3] A. Castellanos, Electrohydrodynamics, Springer, 2014.
[4] D. Das, D. Saintillan, A nonlinear small-deformation theory for transient droplet electrohydrodynamics, J. Fluid Mech. 810 (2017) 225–253.
[5] D. Das, D. Saintillan, Electrohydrodynamics of viscous drops in strong electric fields: numerical simulations, J. Fluid Mech. 829 (2017) 127–152.
[6] W.-F. Hu, M.-C. Lai, Y.-N. Young, A hybrid immersed boundary and immersed interface method for electrohydrodynamic simulations, J. Comput. Phys. 282 (2015) 47–61.
[7] W.-F. Hu, M.-C. Lai, Y. Seol, Y.-N. Young, Vesicle electrohydrodynamic simulations by coupling immersed boundary and immersed interface method, J. Comput. Phys. 317 (2016) 66–81.
[8] H. He, P.F. Salipante, P.M. Vlahovska, Electrorotation of a viscous droplet in a uniform direct current electric field, Phys. Fluids 25 (2013) 032106.
[9] J.-W. Ha, S.-M. Yang, Electrohydrodynamics and electrorotation of a drop with fluid less conductive than that of the ambient fluid, Phys. Fluids 12 (2000) 764.
[10] T.B. Jones, Quincke rotation of spheres, IEEE Trans. Ind. Appl. IA-20 (1984) 845–849.
[11] S. Leung, H. Zhao, A grid based particle method for moving interface problems, J. Comput. Phys. 228 (2009) 2993–3024.
[12] Z. Li, A fast iterative algorithm for elliptic interface problems, SIAM J. Numer. Anal. 35 (1998) 230–254.
[13] Z. Li, K. Ito, The Immersed Interface Method, SIAM, 2006.
[14] J.A. Lanauze, L.M. Walker, A.S. Khair, Nonlinear electrohydrodynamics of slightly deformed oblate drops, J. Fluid Mech. 774 (2015) 245–266.
[15] J.R. Melcher, G.I. Taylor, Electrohydrodynamics: a review of the role of interfacial shear stresses, Annu. Rev. Fluid Mech. 1 (1969) 111–146.
[16] J.R. Melcher, Electric fields and moving media, IEEE Trans. Ed. 17 (1974) 100–110.
[17] H. Nganguia, Y.-N. Young, A.T. Layton, M.-C. Lai, W.-F. Hu, Electrohydrodynamics of a viscous drop with inertia, Phys. Rev. E 93 (2016) 053114.
[18] G. Quincke, Ueber rotationen im constanten electrischen felde, Ann. Phys. 295 (1896) 417.
[19] S.J. Ruuth, B. Merriman, A simple embedding method for solving partial differential equations on surfaces, J. Comput. Phys. 227 (2008) 1943–1961.
[20] A. Ramos (Ed.), Electrokinetics and Electrohydrodynamics in Microsystems, Springer, 2011.
[21] D.A. Saville, Electrohydrodynamics: the Taylor-Melcher leaky dielectric model, Annu. Rev. Fluid Mech. 29 (1997) 27.
[22] C. Sorgentone, A.-K. Tornberg, A highly accurate boundary integral equation method for surfactant-laden drops in 3D, J. Comput. Phys. 360 (2018) 167–191.

[23] P.F. Salipante, P.M. Vlahovska, Electrohydrodynamics of drops in strong uniform dc electric fields, Phys. Fluids 22 (2010) 112110.
[24] P.F. Salipante, P.M. Vlahovska, Electrohydrodynamic rotations of a viscous droplet, Phys. Rev. E 88 (2013) 043003.
[25] S. Santra, S. Mandal, S. Chakraborty, Electrohydrodynamics of confined two-dimensional liquid droplets in uniform electric field, Phys. Fluids 30 (2018) 062003.
[26] G.I. Taylor, Studies in electrohydrodynamics, I: the circulation produced in a drop by an electric field, Proc. R. Soc. Lond. Ser. A, Math. Phys. Sci. 291 (1966) 159.
[27] K.E. Teigen, S.T. Munkejord, Influence of surfactant on drop deformation in an electric field, Phys. Fluids 22 (2010) 112104.
[28] S. Veerapaneni, A. Rahimian, G. Biros, D. Zorin, A fast algorithm for simulating vesicle flows in three dimensions, J. Comput. Phys. 230 (2011) 5610–5634.
[29] S. Xu, An iterative two-fluid pressure solver based on the immersed interface method, Commun. Comput. Phys. 12 (2012) 528–543.
[30] J.-J. Xu, Y. Yang, J. Lowengrub, A level-set continuum method for two-phase flows with insoluble surfactant, J. Comput. Phys. 231 (2012) 5897–5909.
[31] X. Yang, X. Zhang, Z. Li, G.-W. He, A smoothing technique for discrete delta functions with application to immersed boundary method in moving boundary simulations, J. Comput. Phys. 228 (2009) 7821–7836.
[32] H. Zhou, C. Pozrikidis, Deformation of liquid capsules with incompressible interfaces in simple shear flow, J. Fluid Mech. 283 (1995) 175–200.